fractal and fractional

Article

Fractional-Order Zener Model with Temperature-Order Equivalence for Viscoelastic Dampers

Kang Xu [1], Liping Chen [2], António M. Lopes [3], Mingwu Wang [1,*], Ranchao Wu [4] and Min Zhu [2]

[1] School of Civil and Hydraulic Engineering, Hefei University of Technology, Hefei 230009, China; 2019010048@mail.hfut.edu.cn
[2] School of Electrical Engineering and Automation, Hefei University of Technology, Hefei 230009, China; lip_chen@hfut.edu.cn (L.C.); zhumin@hfut.edu.cn (M.Z.)
[3] LAETA/INEGI, Faculty of Engineering, University of Porto, Rua Dr. Roberto Frias, 4200-465 Porto, Portugal; aml@fe.up.pt
[4] School of Mathematics, Anhui University, Hefei 230601, China; rcwu@ahu.edu.cn
* Correspondence: mingwu_wang@hfut.edu.cn

Abstract: Viscoelastic (VE) dampers show good performance in dissipating energy, being widely used for reducing vibration in engineering structures caused by earthquakes and winds. Experimental studies have shown that ambient temperature has great influence on the mechanical behavior of VE dampers. Therefore, it is important to accurately model VE dampers considering the effect of temperature. In this paper, a new fractional-order Zener (AEF-Zener) model of VE dampers is proposed. Firstly, the important influence of fractional orders on the energy dissipation ability of materials is analyzed. Secondly, an equivalent AEF-Zener model is developed that incorporates the ambient temperature and fractional-order equivalence principle. Finally, the chaotic fractional-order particle swarm optimization (CFOPSO) algorithm is used to determine the model's parameters. The accuracy of the AEF-Zener model is verified by comparing model simulations with experimental results. This study is helpful for designing and analyzing vibration reduction techniques for civil structures with VE dampers under the influence of temperature.

Keywords: viscoelastic damper; energy dissipation; temperature-order equivalent principle; fractional-order vibration system

Citation: Xu, K .; Chen, L.; Lopes, A.M.; Wang, M.; Wu, R.; Zhu, M. Fractional-Order Zener Model with Temperature-Order Equivalence for Viscoelastic Dampers. *Fractal Fract.* **2023**, *7*, 714. https://doi.org/10.3390/fractalfract7100714

Academic Editors: Faranak Rabiei, Dongwook Kim and Zeeshan Ali

Received: 1 September 2023
Revised: 23 September 2023
Accepted: 26 September 2023
Published: 28 September 2023

1. Introduction

Earthquakes and wind are among the most catastrophic natural hazards that affect civil engineering structures. Therefore, developing new strategies for protecting building structures from damage caused by disasters has become a very important research topic [1,2]. In recent years, several control methods have been proposed to reduce structural vibrations in civil engineering structures, such as active [3,4], semi-active [5], passive [6,7], and hybrid vibration control [8]. Among them, passive control has been broadly used [9,10]. Indeed, passive vibration control devices emerged as a promising solution, and VE dampers became widely applied in building structures due to their relatively low cost and good energy dissipation performance [11].

Research on VE damping systems focuses on three main aspects, namely (i) development of VE materials with high energy dissipation, (ii) mechanical design, and (iii) analysis of the controlled structures [12,13]. In reference [14], different materials were studied under experimental dynamic loading of full-scale dampers, and a model of the dampers was developed. In references [15,16], the VE parameters of sandwich structures were identified, while a new inverse technique and an adjoint-based gradient method were developed. The dynamics of a structure with VE dampers can be well-described by differential equations of fractional order. The spline collocation method for solving systems of multi-term fractional differential equations was proposed and studied in [17]. In reference [18], several types of VE materials based on different matrix rubbers were optimized and developed, and the mechanical behavior and energy dissipation ability of VE dampers built from these materials were tested. The aforementioned research showed that VE dampers can buffer buildings efficiently against earthquakes due to their large damping capabilities. However, the properties of VE dampers are highly influenced by ambient temperature and excitation frequency, which affect their behavior. Therefore, it is crucial to accurately model VE dampers considering the effect of temperature.

Traditional VE models, such as the Kelvin and Maxwell ones, are unable to accurately capture the frequency-dependent behavior of VE materials [19]. In the past few decades, fractional calculus emerged in scientific and engineering practices [20] due to its ability to model long memory effects, enabling description of the behavior of VE dampers for a wide range of frequencies. Thus, several types of fractional-order constitutive models have been established [21]. However, the effect of ambient temperature on the performance of VE materials is still neglected in most fractional-order models, while in some previous works, it was considered through a shift factor defined by the Williams–Landel–Ferry (WLF) equation [22,23].

The fractional-order Zener model has more degrees of freedom than many other models and can better describe the dynamics of VE materials [24,25]. Indeed, the fractional-order Zener model can well-characterize the influence of frequency [26]. However, it cannot characterize the influence of temperature. In reference [27], a constitutive model was proposed to describe the self-heating effect in elastomeric materials subjected to cyclic loading. In paper [28], the frequency-temperature correspondence principle was adopted, and a method for analyzing the dynamics of structures with VE dampers was addressed. Furthermore, in references [29,30], VE damper models were developed based on molecular chain network micro structures and the temperature-frequency equivalence principle.

In the above references, the influence of temperature usually considers the frequency-temperature equivalence principle. However, temperature and frequency may influence each other, and the physical meaning of equating the influence of temperature to frequency is unclear. Therefore, the accuracy of existing models may be insufficient, and a new approach to effectively model VE dampers is required. In fact, the fractional order has certain geometric and physical significance related to the VE properties of materials [31,32]. A higher order leads to stronger viscosity and stronger energy dissipation, while a lower order causes stronger elasticity and weaker energy dissipation. Therefore, the fractional-order variation in the model can characterize the effect of ambient temperature on the dynamics of VE dampers.

Motivated by the above discussion, a new AEF-Zener model is proposed in this paper. The ability to dissipate energy from VE materials characterized by different fractional orders is analyzed, and the relationship between energy dissipation and fractional order is discussed. Furthermore, based on the temperature-order equivalence, a functional relationship between fractional-order and temperature is established to indirectly characterize the impact of ambient temperature on the performance of VE dampers. The proposed model has a clearer physical meaning and higher accuracy, especially for characterizing the loss factor parameters related to energy consumption, compared to other existing models.

The most important contributions of the paper are:

(a) The influence of fractional order on the energy dissipation capabilities of VE materials is analyzed in the time and frequency domains.
(b) A novel AEF-Zener model is proposed, and the model's parameters are determined by using a CFOPSO algorithm.
(c) The accuracy and effectiveness of the AEF-Zener model is verified by comparing model simulations with experimental results and with models that use the temperature-frequency equivalent principle.

The paper is structured into seven main parts. Section 2 recalls some elemental concepts of fractional calculus. Section 3 presents the mathematical equations of fractional-order Zener VE dampers. Section 4 analyzes the influence of fractional orders. Sections 5 and 6 describe and determine the AEF-Zener model and its parameters, respectively. Section 7 draws the conclusions.

2. Preliminary Concepts of Fractional Calculus

Fractional calculus emerged as an important tool with applications in scientific and engineering fields [33–36]. Some basic definitions concerning fractional calculus are given here for understanding later calculations and analysis.

Given a function $x(t) : R \to R$, it is referred to as C^k-class if its derivatives $x^{(1)}, x^{(2)}, \ldots,$ $x^{(k)}$ exist and are continuous (except for a finite number of points). In the following, we adopt the notation $x(t) \in C^0, C^1$, and C^∞ to denote the classes of all continuous, continuously differentiable, and smooth functions, respectively [37].

The Riemann–Liouville fractional integral of order $\alpha > 0$ of a continuous function $x(t)$ is [38]:

$$
{}_0I_t^\alpha x(t) = D^{-\alpha}x(t) = \frac{1}{\Gamma(\alpha)}\int_0^t (t-s)^{\alpha-1}x(s)ds, \tag{1}
$$

where $\Gamma(\cdot)$ is the gamma function.

The Riemann–Liouville fractional derivative of order $n-1 < \alpha < n$, $n \in N$, of a continuous function $x(t) \in C^n[0,\ t]$ is [39]:

$$
{}_0^{RL}D_t^\alpha x(t) = \frac{1}{\Gamma(n-\alpha)}\frac{d^n}{dt^n}\int_0^t (t-s)^{n-\alpha-1}x(s)ds. \tag{2}
$$

In discrete time, the Grünwald–Letnikov fractional derivative of order $\alpha 0$ of a function $x(t)$ can be approximated by the truncated series [40]:

$$
{}_0^{GL}D_t^\alpha x(t) \approx \frac{1}{T^\alpha}\sum_{k=0}^{r}\frac{(-1)^k\Gamma(\alpha+1)x(t-kT)}{\Gamma(k+1)\Gamma(\alpha-k+1)}, \tag{3}
$$

where r is the truncation value, and T corresponds to the sampling period, respectively.

If $x(t) \in C^n[0,\ t]$, then [37]:

$$
{}_0^{RL}D_t^\alpha x(t) = {}_0^{GL}D_t^\alpha x(t). \tag{4}
$$

The Riemann–Liouville fractional derivative verifies [41]:

$$
\frac{d^n}{dt^n}\left({}_0^{RL}D_t^\alpha x(t)\right) = {}_0^{RL}D_t^\alpha\left(\frac{d^n x(t)}{dt^n}\right) = {}_0^{RL}D_t^{(\alpha+n)}x(t). \tag{5}
$$

For zero initial conditions in the Laplace domain, we have [42]:

$$
L(D^\alpha x(t)) = s^\alpha x(s). \tag{6}
$$

3. Equation of Fractional-Order Zener VE Damper

3.1. Dynamic Equation in the Time Domain

The relationship between strain $\sigma(t)$ and stress $\gamma(t)$ is characterized by the following fractional-order Zener constitutive equation (see Figure 1) :

$$
\sigma(t) + p_1D^\alpha\sigma(t) = q_0\gamma(t) + q_1D^\alpha\gamma(t), \tag{7}
$$

where $\alpha \in (0,1)$ is the order of the Riemann–Liouville fractional differentiation (Equation (2)), and p_1, q_0, and q_1 are positive constant coefficients determined by the VE material's performance parameters E_1, E_2, and η.

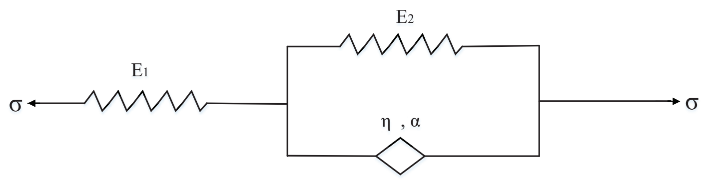

Figure 1. Fractional-order Zener model.

Figure 2 illustrates a one-degree-of-freedom fractional-order Zener damper system consisting of a mass and a damper. The strain and the stress are determined as:

$$\sigma(t) = \frac{f_d(t)}{A}, \gamma(t) = \frac{x(t)}{L}. \tag{8}$$

Combining Equations (7) and (8) results in:

$$f_d(t) + p_1 D^\alpha f_d(t) = \frac{Aq_0}{L} x(t) + \frac{Aq_1}{L} D^\alpha x(t), \tag{9}$$

where L and A stand for length and area, respectively, $f_d(t)$ denotes the damping force, and $x(t)$ represents the displacement of the damper.

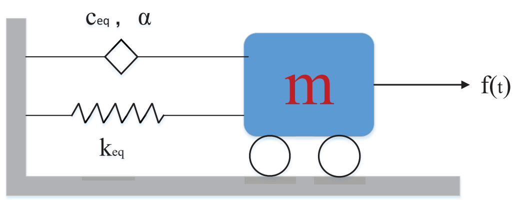

Figure 2. A single-degree-of-freedom fractional Zener VE damper system.

By Newton's second law, the dynamic equation of the damper is:

$$m\ddot{x}(t) + f_d(t) = f(t). \tag{10}$$

From Equations (10) and (5), one has:

$$p_1 m D^{2+\alpha} x(t) + p_1 D^\alpha f_d(t) = p_1 D^\alpha f(t). \tag{11}$$

Equations (10) and (11) give:

$$p_1 m D^{2+\alpha} x(t) + m\ddot{x}(t) + f_d(t) + p_1 D^\alpha f_d(t) = p_1 D^\alpha f(t) + f(t). \tag{12}$$

Substituting Equation (9) into (12) and letting $k = Aq_0/L$ and $c = Aq_1/L$ leads to:

$$p_1 m D^{2+\alpha} x(t) + m\ddot{x}(t) + cD^\alpha x(t) + kx(t) = p_1 D^\alpha f(t) + f(t), \tag{13}$$

where $f(t)$ is the disturbance force, and p_1 falls into either Case 1 or Case 2:

Case 1. If $p_1 = 0$ or $p_1 \to 0$, then Equation (13) can be rewritten as:

$$m\ddot{x}(t) + cD^\alpha x(t) + kx(t) = f(t); \tag{14}$$

Case 2. If $p_1 > 0$, with the following state transformation, then:

$$x(t) = p_1 D^\alpha y(t) + y(t). \tag{15}$$

Substituting Equation (15) into Equation (13) leads to:

$$mp_1D^{2+\alpha}y(t) + m\ddot{y}(t) + cD^{\alpha}y(t) + ky(t) = f(t). \tag{16}$$

With $mp_1D^{2+\alpha}y(t) + m\ddot{y}(t) = m\ddot{x}(t)$, let $cD^{\alpha}y(t) = c^{'}D^{\alpha}x(t)$, $ky(t) = k^{'}x(t)$, Equation (16) can be equivalently transformed into:

$$m\ddot{x}(t) + c^{'}D^{\alpha}x(t) + k^{'}x(t) = f(t). \tag{17}$$

From the above, we establish the equivalent dynamic equation of the fractional-order Zener VE damper with a single degree of freedom:

$$\begin{cases} m\ddot{x}(t) + c_{eq}D^{\alpha}x(t) + k_{eq}x(t) = f(t), \\ f_d(t) = k_{eq}x(t) + c_{eq}D^{\alpha}x(t), \end{cases} \tag{18}$$

where c_{eq} is the damping, and k_{eq} is the equivalent stiffness, which are related to the values of α, p_1, q_0, q_1, frequency ω, and temperature T. We usually analyze them in the frequency domain.

3.2. Dynamic Equation in the Frequency Domain

The Laplace transform (Equation (6)) on Equation (7) results in:

$$\sigma(s) + p_1s^{\alpha}\sigma(s) = q_0\gamma(s) + q_1s^{\alpha}\gamma(s). \tag{19}$$

Therefore, the transfer function of Equation (19) is:

$$G(s) = \frac{\sigma(s)}{\gamma(s)} = \frac{q_0 + q_1s^{\alpha}}{1 + p_1s^{\alpha}}. \tag{20}$$

By replacing s with $i\omega$, with $i^{\alpha} = \cos(\alpha\pi/2) + i \cdot \sin(\alpha\pi/2)$, we obtain the complex modulus:

$$G^{*}(\omega) = G_1(\omega) + iG_2(\omega), \tag{21}$$

where $i = \sqrt{-1}$, and the storage and loss modulus, $G_1(\omega)$ and $G_2(\omega)$, are the real and imaginary components of the complex modulus, respectively. Hence, we have:

$$\begin{cases} G_1(\omega) = \dfrac{\left[q_0 + p_1q_1\omega^{2\alpha} + (q_1 + p_1q_0)\omega^{\alpha}\cos\frac{\alpha\pi}{2}\right]}{\left[1 + p_1^2\omega^{2\alpha} + 2p_1\omega^{\alpha}\cos\frac{\alpha\pi}{2}\right]}, \\ G_2(\omega) = \dfrac{(q_1 - p_1q_0)\omega^{\alpha}\sin\frac{\alpha\pi}{2}}{\left[1 + p_1^2\omega^{2\alpha} + 2p_1\omega^{\alpha}\cos\frac{\alpha\pi}{2}\right]}, \\ \eta = \dfrac{(q_1 - p_1q_0)\omega^{\alpha}\sin\frac{\alpha\pi}{2}}{\left[q_0 + p_1q_1\omega^{2\alpha} + (q_1 + p_1q_0)\omega^{\alpha}\cos\frac{\alpha\pi}{2}\right]}, \end{cases} \tag{22}$$

where $\eta = G_2(\omega)/G_1(\omega)$ is the loss factor.

Then, the mechanical properties of the VE damper, namely the equivalent stiffness and damping, k_{eq} and c_{eq}, respectively, can be calculated and analyzed with the following equations:

$$k_{eq}^{'} = \frac{n_v \cdot G_1 \cdot A_v}{h_v}, \tag{23}$$

$$c_{eq}^{'} = \frac{n_v \cdot G_2 \cdot A_v}{\omega \cdot h_v}, \tag{24}$$

where n_v is the number of layers of VE material between the steel plates that compose the VE damper, and A_v and h_v are the shear area and thickness of each VE layer, respectively.

4. The Influence of Fractional-Order α

Numerical simulations are carried out to demonstrate the influence of the fractional order α on the VE damper energy dissipation capacity. From Section 3, one can observe that the fractional order α is related to the dynamic properties of the VE material in the time and frequency domains.

4.1. Analysis in the Time Domain

The coefficients in the fractional-order model of the Zener VE damper (Equation (18)) are taken as $m = 1, c_{eq} = 0.5, k_{eq} = 1$, and $\alpha \in (0, 1)$, and the disturbance is assumed to be a step signal:

$$f(t) = \begin{cases} 0, & 0 < t < 1, \\ 10, & 1 \leq t. \end{cases} \tag{25}$$

It follows from Equation (18) that:

$$x(t) = \frac{1}{k_{eq}}(f(t) - m\ddot{x}(t) - c_{eq} \cdot {}_{RL}D^{\alpha}x(t)). \tag{26}$$

Figure 3 illustrates the Simulink block diagram programming adopted for the fractional-order equation with zero initial values. The fractional-order operator D^{α} can be approximated using MATLAB2019a programming based on Equations (3) and (4). Vibration responses of the fractional-order Zener VE damper with different fractional orders are shown in Figure 4. One can see that the energy dissipation capacity of the VE damper is stronger with the increase in the fractional order α.

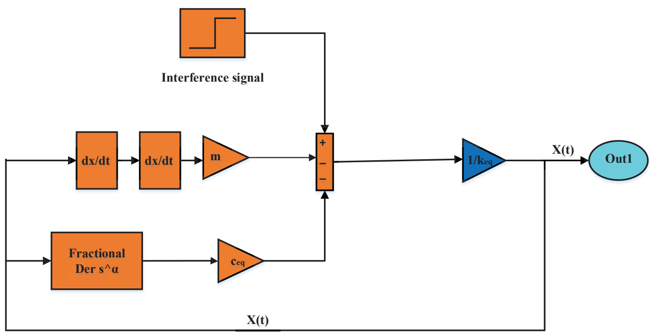

Figure 3. Simulink block diagram for the fractional equation with zero initial values.

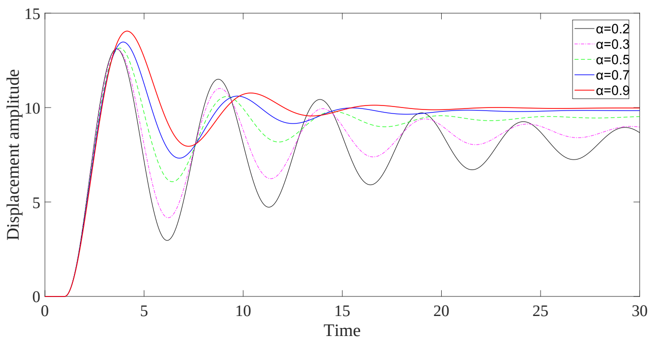

Figure 4. Vibration responses of the fractional Zener VE damper with different fractional order α.

4.2. Analysis in the Frequency Domain

In this simulation, the coefficients of the fractional-order Zener VE damper (Equation (22)) are taken as $p_1 = 0.0015, q_0 = 0.5, q_1 = 1.25, \omega \in (0.1, 2]$, and $\alpha \in (0, 1)$.

The responses of the storage modulus and loss factor, G_1 and η, respectively, of the fractional-order Zener VE damper with different fractional orders are shown in Figures 5 and 6, respectively. Figures 7 and 8 show two responses with different fractional orders and frequencies. From Figures 5 and 6, we verify that the fractional order α has a positive correlation with the change in G_1 and a negative correlation with the change in η. Figures 7 and 8 indicate that frequency also has a great influence on the dynamic performance of the damper.

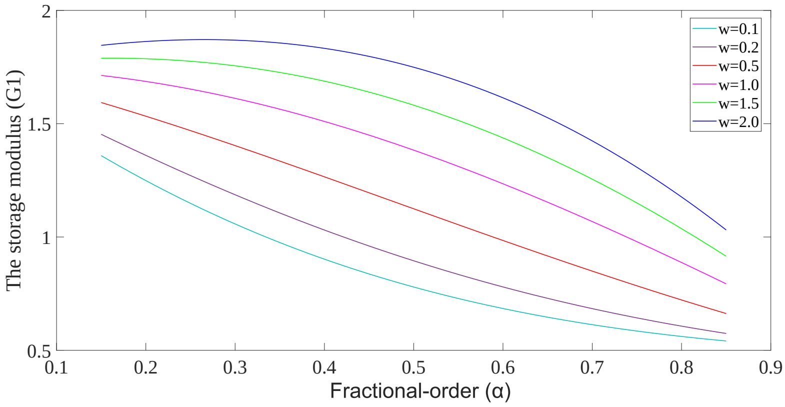

Figure 5. The storage modulus G_1 of the VE damper at different frequencies and fractional orders.

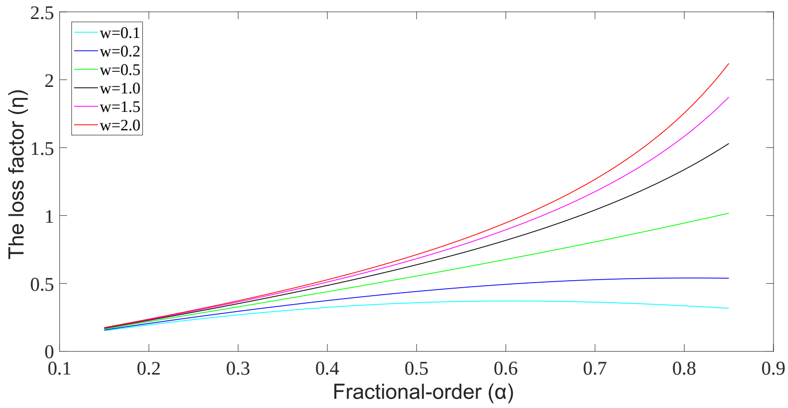

Figure 6. The loss factor η of the VE damper at different frequencies and fractional orders.

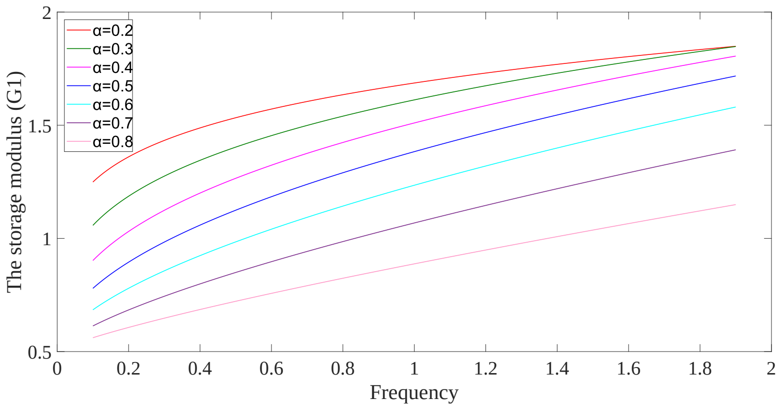

Figure 7. The storage modulus G_1 of the VE damper at different fractional orders and frequencies.

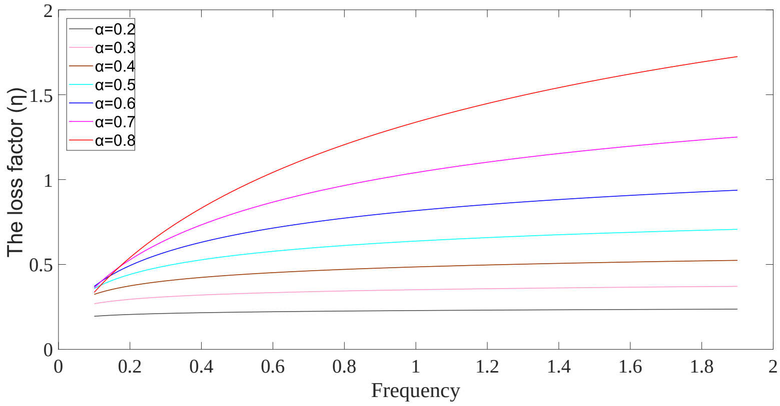

Figure 8. The loss factor η of the VE damper at different fractional orders and frequencies.

The above simulations confirm that the fractional order α is related to the energy dissipation capacity and dynamic performance of the damper. The higher the order is, the stronger the viscosity and the energy dissipation are.

5. Temperature-Order Equivalent Mathematical Model

5.1. Temperature-Order Equivalent Principle

Experimental results show that temperature and frequency affect the dynamics of VE dampers and that temperature has a more prominent effect, as illustrated in Figures 9 and 10 [29]. From Equation (22), it can be seen that the influence of frequency is described well. However, the fractional-order Zener model can not characterize the effect of temperature. Therefore, we establish the necessary relationship by introducing a new mathematical model that considers the temperature change and fractional-order equivalence, given by:

$$\begin{cases} G_1(\omega, T) = G_1(\omega, \alpha_1(T)), \\ \eta(\omega, T) = \eta(\omega, \alpha_2(T)), \end{cases} \tag{27}$$

where α_1 and α_2 are:

$$\begin{cases} \alpha_1(T) = \sum_{i=1}^{5} a_i T^i + b_1, \\ \alpha_2(T) = 1 - (\sum_{i=1}^{5} c_i T^i + b_2). \end{cases} \tag{28}$$

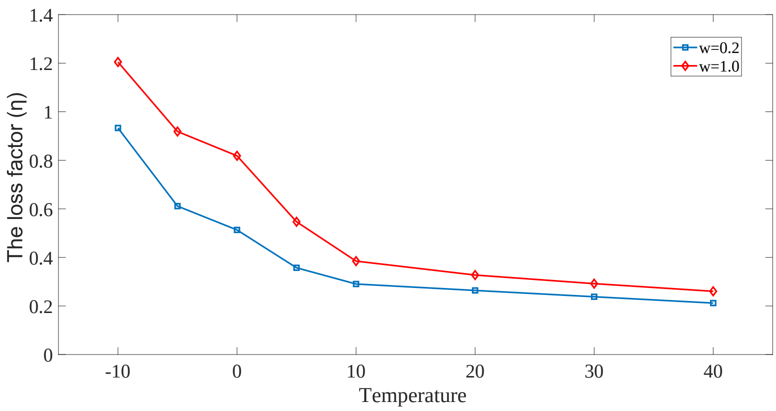

Figure 9. The loss factor η of the VE damper at different temperatures.

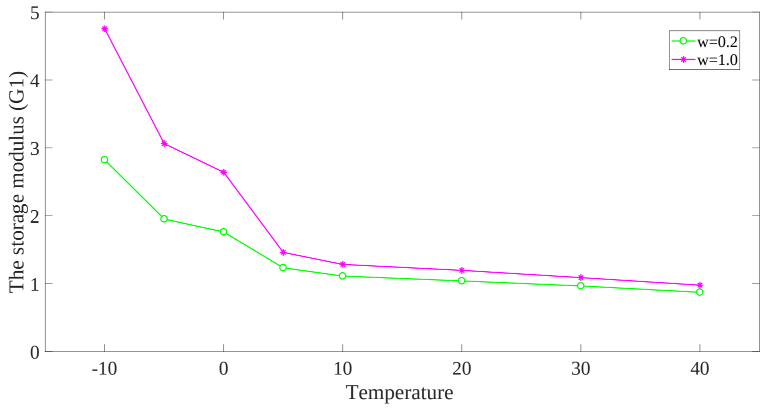

Figure 10. The storage modulus G_1 of the VE damper at different temperatures.

Thus, Equation (22) can be rewritten as:

$$\begin{cases} G_1 = \dfrac{\left[q_0 + p_1 q_1 \omega^{2\alpha_1} + (q_1 + p_1 q_0)\omega^{\alpha_1} \cos \frac{\alpha_1 \pi}{2}\right]}{\left[1 + p_1^2 \omega^{2\alpha_1} + 2p_1 \omega^{\alpha_1} \cos \frac{\alpha_1 \pi}{2}\right]}, \\ \eta = G_2/G_1 = \dfrac{(q_1 - p_1 q_0)\omega^{\alpha_2} \sin \frac{\alpha_2 \pi}{2}}{\left[q_0 + p_1 q_1 \omega^{2\alpha_2} + (q_1 + p_1 q_0)\omega^{\alpha_2} \cos \frac{\alpha_2 \pi}{2}\right]}. \end{cases} \tag{29}$$

5.2. Model Modification

As the influence of temperature on the properties of VE dampers is related to frequency, the temperature and fractional-order equivalent relationship with frequency correction can be obtained as:

$$\begin{cases} G_1(\omega, T) = G_1(\omega, \alpha_1^*(T, \omega)), \\ \eta(\omega, T) = \eta(\omega, \alpha_2^*(T, \omega)). \end{cases} \tag{30}$$

For simplifying the analysis, we first fix $\omega = 0.5$. Then, α_1^* and α_2^* are calculated as:

$$\begin{cases} \alpha_1^*(T, \omega) = \alpha_1(T, 0.5) + k_1(\omega - 0.5), \\ \alpha_2^*(T, \omega) = \alpha_2(T, 0.5) - k_2(\omega - 0.5), \end{cases} \tag{31}$$

where k_1 and k_2 are determined by:

$$\begin{cases} k_1 = \sum_{i=1}^{5} a_i^* T^i + b_1^*, \\ k_2 = \sum_{i=1}^{5} c_i^* T^i + b_2^*. \end{cases} \tag{32}$$

Therefore, by considering the temperature effect and the frequency modified model, the new AEF-Zener model is given by:

$$\begin{cases} G_1 = \dfrac{\left[q_0 + p_1 q_1 \omega^{2\alpha_1^*} + (q_1 + p_1 q_0)\omega^{\alpha_1^*} \cos \frac{\alpha_1^* \pi}{2}\right]}{\left[1 + p_1^2 \omega^{2\alpha_1^*} + 2p_1 \omega^{\alpha_1^*} \cos \frac{\alpha_1^* \pi}{2}\right]}, \\ \eta = G_2/G_1 = \dfrac{(q_1 - p_1 q_0)\omega^{\alpha_2^*} \sin \frac{\alpha_2^* \pi}{2}}{\left[q_0 + p_1 q_1 \omega^{2\alpha_2^*} + (q_1 + p_1 q_0)\omega^{\alpha_2^*} \cos \frac{\alpha_2^* \pi}{2}\right]}. \end{cases} \tag{33}$$

Further, we have:

$$k'_{eq} = \frac{n_v \cdot G_1(\omega, \alpha^*) \cdot A_v}{h_v}, \tag{34}$$

$$c'_{eq} = \frac{n_v \cdot G_2(\omega, \alpha^*) \cdot A_v}{\omega \cdot h_v}, \tag{35}$$

where the values of parameters p_1, q_0, q_1, α_1^*, and α_2^* in Equation (33) are used to define the material properties. It should be noted that this model reflects the impact of ambient temperature on the dynamic behaviors of the VE dampers through the fractional order.

6. Parameter Identification and Experimental Comparison

In this section, the storage modulus and loss factor, G_1 and η, respectively, that represent the mechanical properties of the VE damper are used to determine the parameters of the equivalent model. The experimental data from the dynamic tests in reference [29] were used. Herein, we propose a new chaotic fractional-order particle swarm optimization (CFOPSO) algorithm to accurately determine the model's parameters.

6.1. Parameter Identification with the CFOPSO

The PSO is a simple and easy-to-implement algorithm. The PSO can be generalized using fractional-order tools to yield the fractional-order PSO algorithm, which can better balance global and local searching capabilities [43]. Chaotic mapping can be used to generate evenly chaotic numbers between 0 and 1, as shown in Figure 11. The population initialization is carried out by using chaotic sequences contributing to an increase in the performance of the algorithm [44]. The values are mapped to initialization particle individuals according to the following formula:

$$\begin{cases} y_{i+1} = \mu y_i (1 - y_i), \\ \quad \chi = \chi_{Lb} + (\chi_{Ub} - \chi_{Lb}) y_{i+1}, \end{cases} \tag{36}$$

where i is the number of iterations, and μ is the bifurcation parameter. The symbols χ_{Ub} and χ_{Lb} are the upper and lower limits of each individual in each dimension, and y_{i+1} is the mapped individual.

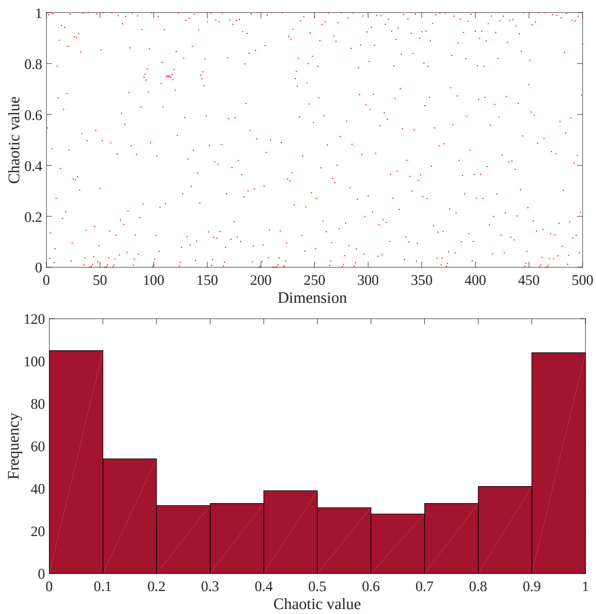

Figure 11. Chaotic mapping generating chaotic numbers.

The velocity and position of the particles are updated using:

$$\begin{cases} D^{\alpha} v_{ij}(t+1) = c_1 \phi_1 [Pb_{ij}(t) - \chi_{ij}(t)] + c_2 \phi_2 [Gb_{gj}(t) - \chi_{ij}(t)], \\ \quad \chi_{ij}(t+1) = \chi_{ij}(t) + v_{ij}(t+1), \end{cases} \tag{37}$$

where $Pb_{ij}(t)$ is its best position for each particle found so far, $Gb_{gj}(t)$ is the best position of the swarm, c_1 and c_2 denote the coefficients of the particle acceleration, and ϕ_1 and ϕ_2 are random numbers in the interval $[0,1]$.

Considering the first four terms of the differential derivative given by Equation (3), one has:

$$\begin{aligned} v_{ij}(t+1) &= \alpha v_{ij}(t) + \frac{1}{2}\alpha(1-\alpha)v_{ij}(t-1) \\ &+ \frac{1}{6}\alpha(1-\alpha)(2-\alpha)v_{ij}(t-2) \\ &+ \frac{1}{24}\alpha(1-\alpha)(2-\alpha)(3-\alpha)v_{ij}(t-3) \\ &+ c_1\phi_1[Pb_{ij}(t) - \chi_{ij}(t)] + c_2\phi_2[Gb_{gj}(t) - \chi_{ij}(t)], \end{aligned} \tag{38}$$

where α at the i-th iteration is:

$$\alpha_i = \alpha_{max} - \frac{\alpha_{max} - \alpha_{min}}{i_{max}} i, \quad \alpha_i \in [0.4, 0.9], \tag{39}$$

with i_{max} denoting the maximum number of iterations.

The parameter values are found by minimizing the fitness function, $f(.)$, which represents the error between the calculated $(G_1(i), \eta(i))$ and experimental $(\widehat{G}_1(i), \widehat{\eta}(i))$ values, as defined in:

$$\min f(\cdot) = \min \sum_{i=1}^{M} \Big[|G_1(i) - \widehat{G}_1(i)| + |\eta(i) - \widehat{\eta}(i)| \Big], \tag{40}$$

where the symbol M is the number of sampling points. Figure 12 schematically illustrates the CFOPSO algorithm. Table 1 lists the parameter values of the CFOPSO algorithm.

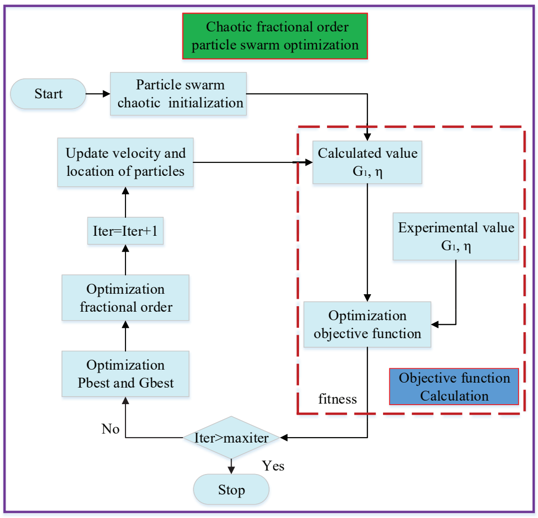

Figure 12. Flowchart of the CFOPSO algorithm.

Table 1. Parameters of the CFOPSO algorithm.

CFOPSO Parameter	Value
Number of particles	$N = 50$
Number of iterations/Repeated experiments	$i = 200/E = 40$
Scaling factors	$c_1 = c_2 = 1.5$
Chaotic bifurcation parameter	$\mu = 4.0$

The experimental data with a displacement of 1.0 mm are adopted for parameter determination and fitting. With reference to the parameter values in previous fractional models, the range of current parameter values is set as $p_1 \in (0, 2.5 \times 10^{-6}]$, $q_0 \in (0, 2]$, $q_1 \in (0, 5]$, $\alpha_1 \in (0, 1)$, and $\alpha_2 \in (0, 1)$. The process of model parameter determination and fitting is:

Step 1: Determine the parameters p_1, q_0, q_1, α_1, and α_2 in Equation (29) with $T = 10$ °C and $\omega = 0.5$ rad/s using the CFOPSO algorithm;

Step 2: With fixed parameters p_1, q_0, and q_1, determine the values of α_1 and α_2 with $T = -10$ °C, -5 °C, 0 °C, 5 °C, 20 °C, 30 °C, 40 °C, and $\omega = 0.5$ rad/s;

Step 3: Use curve-fitting to find the parameters in the functions that relate α_1 and α_2 to temperature T;

Step 4: Repeat Steps 1 to 3 with $\omega = 0.1$ rad/s, 0.2 rad/s, and 1.0 rad/s, with the fixed parameters p_1, q_0, and q_1;

Step 5: Set the model at $\omega = 0.5$ rad/s as the reference model. Fit the effects of other frequencies into the fractional orders α_1^* and α_2^* through two slope functions. Use curve-fitting to determine the parameters in the functions that relate k_1 and k_2 to temperature T.

Finally, the new AEF-Zener model's parameters in Equation (33) have been determined.

Table 2 lists the parameter values of the AEF-Zener model ($\omega = 0.5$ rad/s) obtained with the CFOPSO algorithm. The values of k_1 and k_2 determined by slope curve-fitting are shown in Table 3.

Table 2. Parameters of the AEF-Zener model ($\omega = 0.5$ rad/s).

Parameters	$\boldsymbol{P_1}$	$\boldsymbol{q_0}$	$\boldsymbol{q_1}$	$\boldsymbol{a_1}$
Values	1.02×10^{-6}	0.651	3.849	-6.82×10^{-9}
Parameters	a_2	a_3	a_4	a_5
Values	4.076×10^{-7}	1.369×10^{-5}	-0.0013	0.0301
Parameters	b_1	c_1	c_2	c_3
Values	0.6526	-7.37×10^{-9}	7.039×10^{-7}	-1.449×10^{-5}
Parameters	c_4	c_5	b_2	
Values	-0.454×10^{-3}	0.0213	0.574	

Table 3. Parameters of the modified AEF-Zener model (k_1, k_2).

Parameters	$\boldsymbol{a_1^*}$	$\boldsymbol{a_2^*}$	$\boldsymbol{a_3^*}$	$\boldsymbol{a_4^*}$
Values	4.911×10^{-8}	-4.656×10^{-6}	1.537×10^{-4}	-0.00212
Parameters	a_5^*	b_1^*	c_1^*	c_2^*
Values	0.00995	0.2227	-4.314×10^{-8}	4.291×10^{-6}
Parameters	c_3^*	c_4^*	c_5^*	b_2^*
Values	0.2227	0.001589	0.004628	-0.1724

6.2. Comparison between Numerical and Experimental Results

To assess the accuracy of the proposed AEF-Zener model, the parameters G_1 and η with varying loading frequencies and ambient temperatures were computed based on Equation (33). The numerical calculations and experimental data are compared in Figures 13–16 and Table 4. It can be seen that the model has high precision.

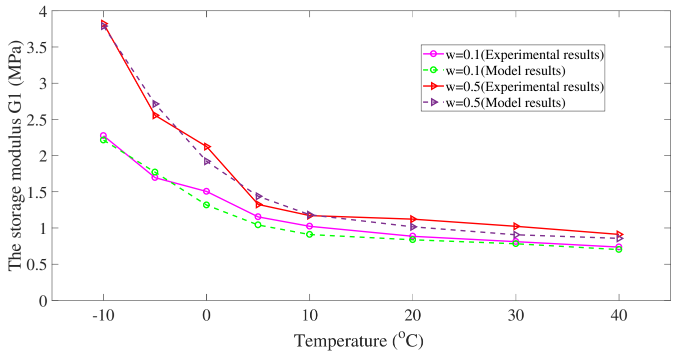

Figure 13. Comparison between numerical and experimental results of G_1 ($\omega = 0.1, 0.5$).

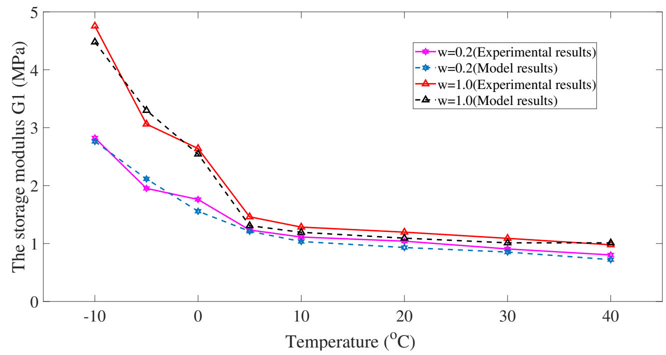

Figure 14. Comparison between numerical and experimental results of G_1 ($\omega = 0.2, 1.0$).

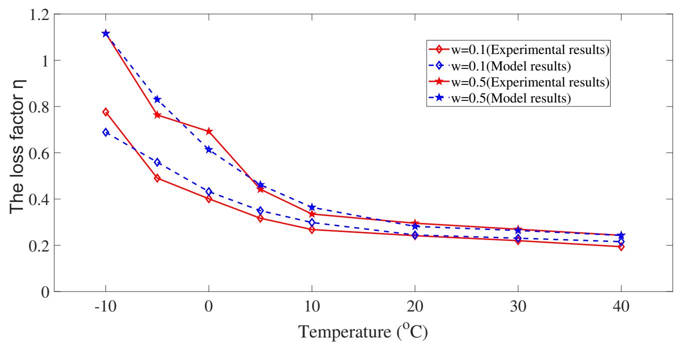

Figure 15. Comparison between numerical and experimental results of η ($\omega = 0.1, 0.5$).

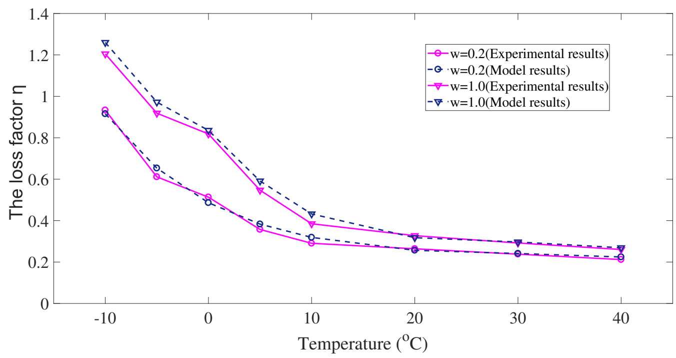

Figure 16. Comparison between numerical and experimental results of η ($\omega = 0.2, 1.0$).

Table 4. Comparison between experimental data and numerical results for the AEF-Zener model.

		Storage Modulus, G_1 (MPa)		**Loss Factor, η**	
ω (rad/s)	**T (°C)**	**Experimental**	**Numerical**	**Experimental**	**Numerical**
	−10	2.2740	2.2129	0.7765	0.6886
	−5	1.6951	1.7699	0.4904	0.5591
	0	1.5043	1.3159	0.4012	0.4321
0.1	5	1.1530	1.0412	0.3170	0.3498
	10	1.0232	0.9092	0.2681	0.2985
	20	1.0037	0.9068	0.2413	0.2447
	30	0.8111	0.7819	0.2201	0.2306
	40	0.7360	0.7014	0.1940	0.2157
	−10	2.8233	2.7623	0.9332	0.9156
	−5	1.9408	2.1160	0.6119	0.6533
	0	1.7612	1.5584	0.5132	0.4863
0.2	5	1.2341	1.2118	0.3573	0.3831
	10	1.1123	1.0350	0.2905	0.3190
	20	1.0481	0.9313	0.2612	0.2566
	30	0.9068	0.8531	0.2380	0.2412
	40	0.8034	0.7221	0.2121	0.2245
	−10	3.8227	3.7887	1.1168	1.1153
	−5	2.5560	2.7139	0.7635	0.8305
	0	2.1240	1.9211	0.6923	0.6135
0.5	5	1.3250	1.4382	0.4423	0.4618
	10	1.1710	1.1824	0.3353	0.3641
	20	1.1262	1.0158	0.2940	0.2817
	30	1.0231	0.9062	0.2693	0.2640
	40	0.9114	0.8565	0.2433	0.2429
	−10	4.7551	4.4795	1.2049	1.2601
	5	3.0626	3.2987	0.9186	0.9722
	0	2.6408	2.5450	0.8185	0.8356
1.0	5	1.4614	1.3090	0.5468	0.5912
	10	1.2840	1.1941	0.3848	0.4322
	20	1.1967	1.0929	0.3274	0.3176
	30	1.0897	1.0123	0.2920	0.2968
	40	0.9786	1.0116	0.2605	0.2690

The root-mean-square errors between numerical and experimental results are given in Table 5. When the frequencies are chosen as $0.1, 0.2, 0.5$, and 1.0 rad/s, the errors for the values of G_1 are 9.65%, 11.16%, 11.63%, and 15.41%, respectively. The errors for η are 4.47%, 2.23%, 3.89%, and 3.64%, respectively. As the frequency increases, its impact on the parameters may increase, which may lead to an increase in errors for high frequencies. In addition, the relative errors of the storage modulus and loss factor, G_1 and η, at various frequencies are less than 20%, which are within the requirements usually adopted in engineering applications.

Table 5. Root-mean-square error of G_1 and η.

	Storage Modulus, G_1	**Loss Factor, η**
Frequency (rad/s)	**Root-Mean-Square Error (%)**	**Root-Mean-Square Error (%)**
0.1	9.65	4.47
0.2	11.16	2.23
0.5	11.63	3.89
1.0	15.41	3.64

To further verify the effectiveness of the AEF-Zener model, taking the frequency of 1.0 rad/s, we compare its results with those of the EFMCS model (that considers the temperature–frequency equivalent principle) [45] and the experimental data. The storage modulus and the loss factor for the displacement of 1.0 mm and temperatures of −10 °C to 40 °C are illustrated in Figures 17 and 18, respectively, and summarized in Tables 6 and 7.

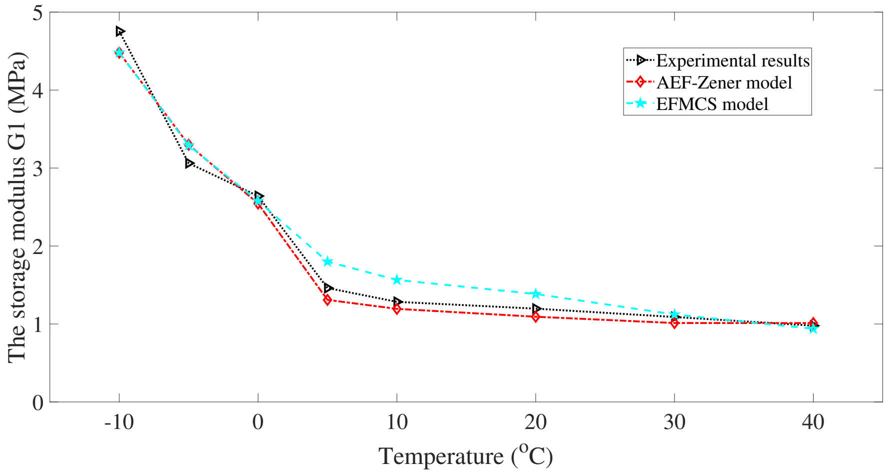

Figure 17. Comparison between numerical and experimental results of G_1 with $T(°C) = -10, -5, 0, 5, 10, 20, 30, 40$ when $d = 1.0$ mm and $\omega = 1.0$ rad/s.

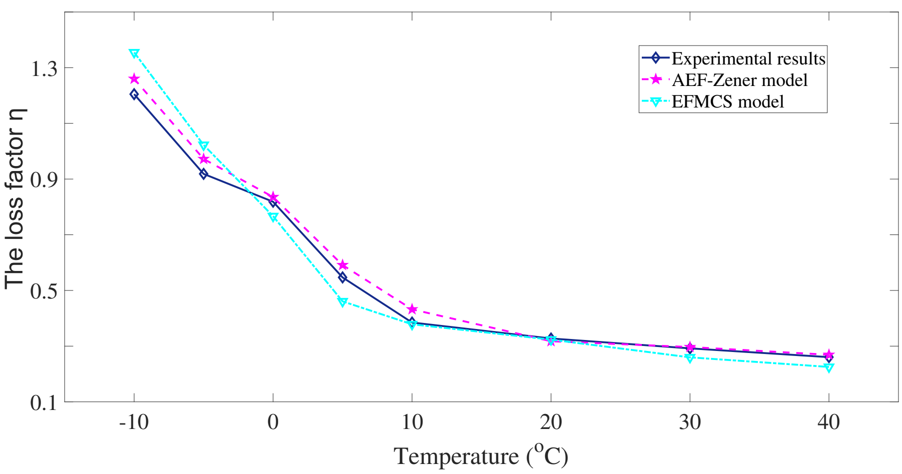

Figure 18. Comparison between numerical and experimental results of η with $T(°C) = -10, -5, 0, 5, 10, 20, 30, 40$ when $d = 1.0$ mm and $\omega = 1.0$ rad/s.

Table 6. The experimental and numerical results comparison of G_1 for different frequencies when $d = 1.0$ mm and $\omega = 1.0$ rad/s.

	Storage Modulus, G_1 (MPa)			**Error**	
T(°C)	**Experimental**	**AEF Model**	**EFMCS Model**	**AEF Model**	**EFMCS Model**
−10	4.7551	4.4795	4.4803	5.80%	5.78%
−5	3.0626	3.2987	3.2900	7.71%	7.41%
0	2.6408	2.5450	2.5777	3.63%	2.39%
5	1.4614	1.3090	1.7995	9.28%	23.14%
10	1.2840	1.1941	1.5653	7.00%	21.73%
20	1.1967	1.0929	1.3847	8.67%	15.71%
30	1.0897	1.0123	1.1218	7.10%	2.95%
40	0.9786	1.0116	0.9389	3.37%	4.06%

Table 7. The experimental and numerical results comparison of η for different frequencies when $d = 1.0$ mm and $\omega = 1.0$ rad/s.

	Loss Factor, η			Error	
T(° C)	**Experimental**	**AEF Model**	**EFMCS Model**	**AEF Model**	**EFMCS Model**
−10	1.2049	1.2601	1.3549	4.58%	7.52%
−5	0.9186	0.9722	1.0225	5.83%	11.31%
0	0.8185	0.8356	0.7666	2.09%	6.34%
5	0.5468	0.5912	0.4608	8.12%	15.73%
10	0.3848	0.4322	0.3784	12.32%	1.66%
20	0.3274	0.3176	0.3234	3.00%	1.22%
30	0.2920	0.2968	0.2597	1.64%	11.06%
40	0.2605	0.2690	0.2253	3.26%	13.51%

For the storage modulus, at different temperatures, the average and the maximum errors between experimental data and simulation results for the AEF-Zener and the EFMCS models are 6.57% and 10.40%, and 9.28% and 23.14%, respectively. For the loss factor, the average and the maximum errors are 5.11% and 8.54%, and 12.32% and 15.73%, respectively. This shows that both errors for the AEF-Zener model are smaller than those for the EFMCS.

Additionally, at the temperature of 20 °C, the AEF-Zener model simulation results are compared with those obtained with Xu's model [29] and with experimental data. Figures 19 and 20 depict the storage modulus and the loss factor when the displacement is 1.0 mm and the frequencies vary between 0.1 rad/s and 1.0 rad/s, respectively. Tables 8 and 9 summarize the results.

For the storage modulus, the average and the maximum errors for the AEF-Zener and the Xu models are 7.23% and 9.34%, and 11.14% and 11.80%, respectively. For the loss factor, the errors are 2.59% and 3.90%, and 4.18% and 9.07%, respectively. This confirms that the AEF-Zener model is better than the Xu model.

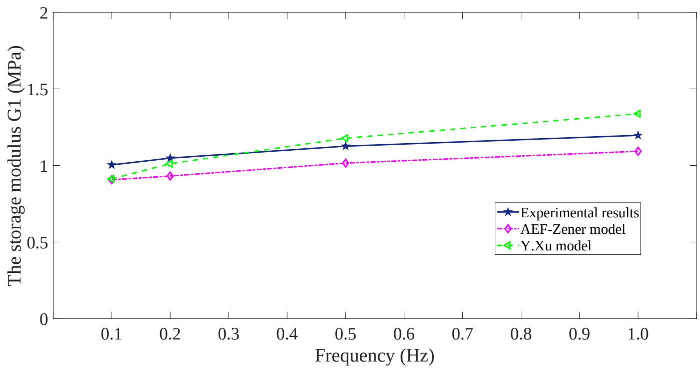

Figure 19. Comparison of numerical and experimental results of G_1 with $\omega = 0.1, 0.2, 0.5, 1.0$ when $d = 1.0$ mm and $T = 20$ °C.

Table 8. The experimental and numerical results comparison of G_1 for different frequencies when $d = 1.0$ mm and $T = 20$ °C.

	Storage Modulus, G_1 (MPa)			Error	
ω (rad/s)	**Experimental**	**AEF Model**	**Xu's Model**	**AEF Model**	**Xu's Model**
0.1	1.0037	0.9068	0.9128	9.65%	9.05%
0.2	1.0481	0.9313	1.0119	11.14%	3.45%
0.5	1.1262	1.0158	1.1784	9.80%	4.63%
1.0	1.1967	1.0929	1.3379	8.67%	11.80%

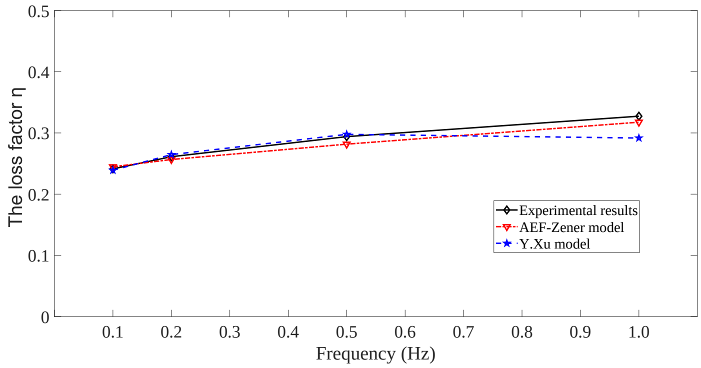

Figure 20. Comparison of numerical and experimental results of η with $\omega = 0.1, 0.2, 0.5, 1.0$ when $d = 1.0$ mm and $T = 20$ °C.

Table 9. The experimental and numerical results comparison of η for different frequencies when $d = 1.0$ mm and $T = 20$ °C.

	Loss Factor, η			**Error**	
ω (rad/s)	**Experimental**	**AEF Model**	**Xu's Model**	**AEF Model**	**Xu's Model**
0.1	0.2413	0.2447	0.2390	1.41%	0.95%
0.2	0.2612	0.2566	0.2646	1.76%	1.30%
0.5	0.2940	0.2817	0.2977	4.18%	4.28%
1.0	0.3274	0.3176	0.2917	2.99%	9.07%

From the above analysis, we verify that the numerical results obtained with the proposed AEF-Zener model are close to the experimental ones, which means that the temperature-order equivalence principle can well characterize the effect of temperature for VE dampers. In addition, by comparing the new model with the EFMCS and the Xu models, we confirmed that the AEF-Zener model has superior accuracy and availability. In general, the AEF-Zener model is accurate enough to reflect the mechanical behavior and energy dissipation ability of VE dampers at a low frequency. The model can be conveniently applied to the dynamic analysis of structures with VE dampers.

7. Simulation Analysis of Structures with VE Dampers

In this section, simulations of structures with and without VE dampers under earthquake action are carried out. The equation of motion of the structure with VE dampers can be written as:

$$M\ddot{x}(t) + C\dot{x}(t) + Kx(t) + c_d\dot{x}(t) + k_d x(t) = -Ml\ddot{x}_g, \tag{41}$$

where x, $\dot{x}$, and $\ddot{x} \in R^{n\times 1}$ stand for displacement, velocity, and acceleration vectors of the building, respectively; M, C, and $K \in R^{n\times n}$ are the mass, stiffness, and damping matrices, respectively; l is a vector with all elements equal to 1; and $k_d = \mathrm{diag}(k_{di}, \ldots, k_{dn})$ and $c_d = \mathrm{diag}(c_{di}, \ldots, c_{dn})$, with k_{di} and c_{di} standing for the sum of equivalent stiffness and damping of all VE dampers in the i-th floor for $i = 1, \ldots, n$, are parameters.

The ground acceleration $\ddot{x}_g$ is modulated with amplitude 0.24 g and 0.12 g to adopt the El Centro and Taft earthquake seismic waves for 25 s and 30 s, as shown in Figure 21. In addition, the Rayleigh damping is given by $C = \alpha_1 M + \beta_1 K$, where $\alpha_1, \beta_1 \in R$ are calculated from the damping ratio of the modes of vibration. Matrices M and K can be represented by:

$$M = \begin{bmatrix} m_1 & 0 & \cdots & 0 & 0 \\ 0 & m_2 & \cdots & 0 & 0 \\ \vdots & \vdots & \vdots & \ddots & \vdots \\ 0 & 0 & \cdots & m_{n-1} & 0 \\ 0 & 0 & \cdots & 0 & m_n \end{bmatrix}_{n\times n},$$

$$K = \begin{bmatrix} k_1+k_2 & -k_2 & \cdots & 0 & 0 \\ -k_2 & k_2+k_3 & \cdots & 0 & 0 \\ \vdots & \vdots & \ddots & \vdots & \vdots \\ 0 & 0 & \cdots & k_{n-1}+k_n & -k_n \\ 0 & 0 & \cdots & -k_n & k_n \end{bmatrix}_{n\times n}.$$

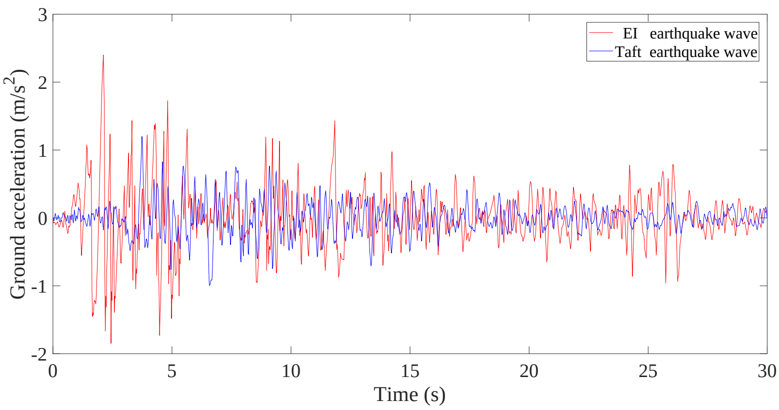

Figure 21. El-Centro and Taft earthquake seismic waves.

Example : The application of the AEF-Zener model for a three-story building structure with 10 VE dampers on each story is illustrated in Figure 22. The parameters of the structure are summarized in Table 10. The sizes of the VE dampers are $n_v = 2$, $A_v = 0.36$ m^2, and $h_v = 10$ mm, respectively. The VE dampers can be placed in any location where shear deformation of the VE layers is allowed to occur. The ambient temperature is set as $T = 7.3$ °C. The first natural frequency of the vibration mode is $\omega = 0.881$ rad/s. Equations (33)–(35) can be used to calculate the equivalent stiffness and damping.

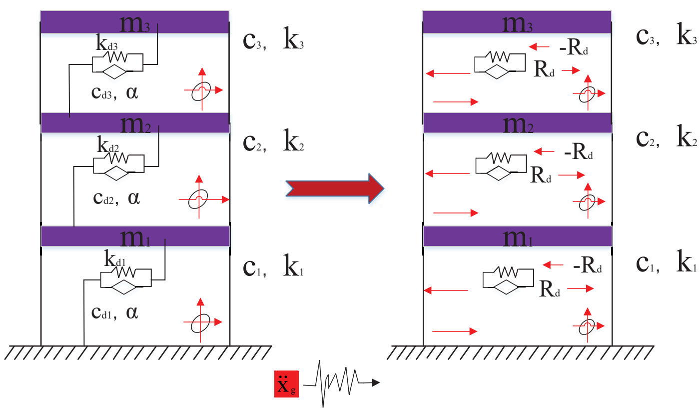

Figure 22. A three-story building with VE dampers.

Table 10. Building parameters for the example.

Floor	1	2	3
Quality (kg)	2.40×10^5	1.20×10^5	1.20×10^5
Rigidity (N/m)	1.08×10^6	3.60×10^5	2.16×10^5

Figures 23–25 show the displacements of the first to third floors, without and with VE dampers, respectively, in the El Centro earthquake. Figure 26 show the maximum displacements in the El-Centro earthquake. The corresponding floor displacements in the Taft earthquake are shown in Figures 27–29, respectively. Figure 30 show the maximum displacements in the Taft earthquake.

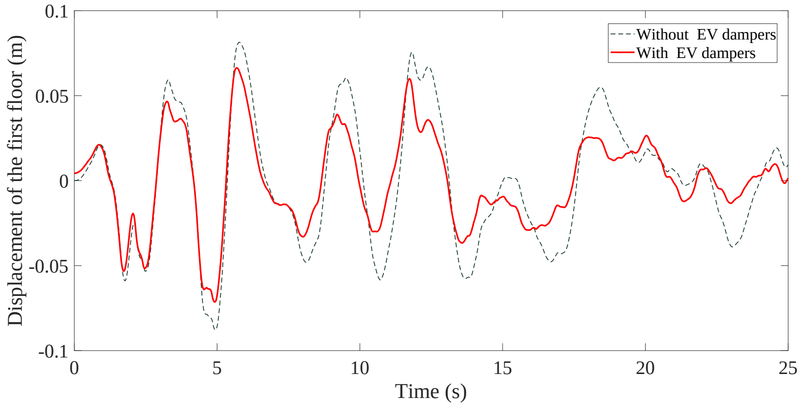

Figure 23. First floor displacement of the building in the example in the El Centro earthquake.

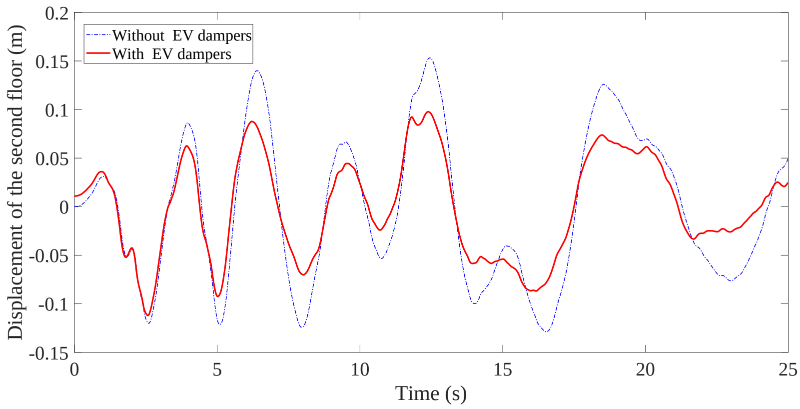

Figure 24. Second floor displacement of the building in the example in the El Centro earthquake.

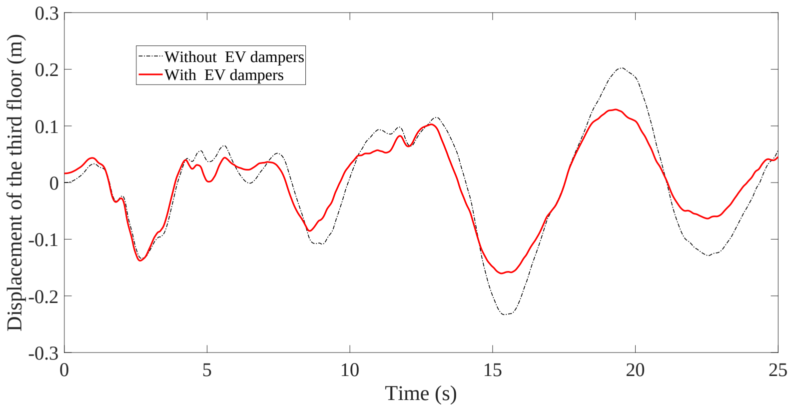

Figure 25. Third floor displacement of the building in the example in the El Centro earthquake.

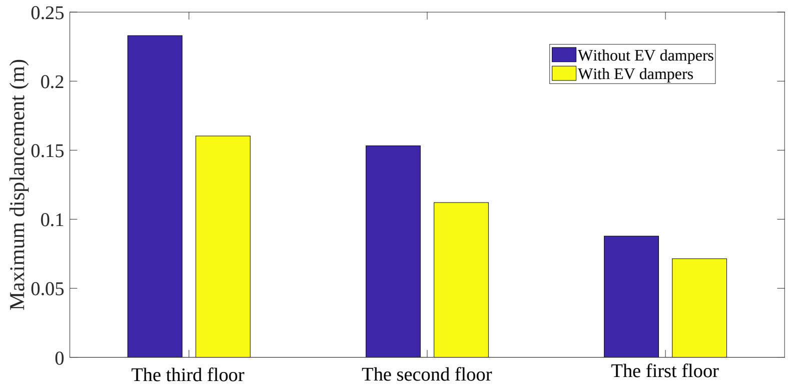

Figure 26. The maximum displacement of each floor in the El Centro earthquake.

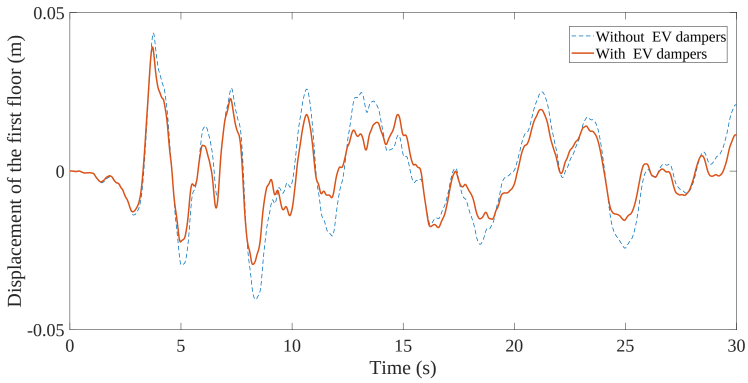

Figure 27. First floor displacement of the building in the example in the Taft earthquake.

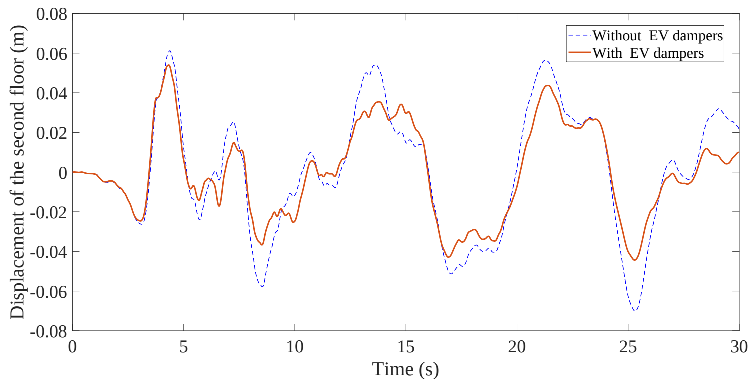

Figure 28. Second floor displacement of the building in the example in the Taft earthquake.

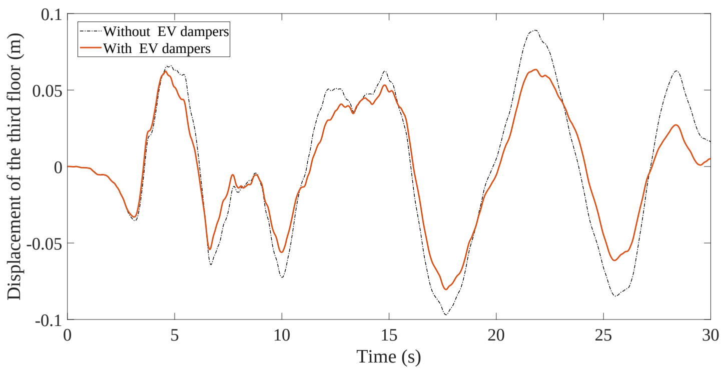

Figure 29. Third floor displacement of the building in the example in the Taft earthquake.

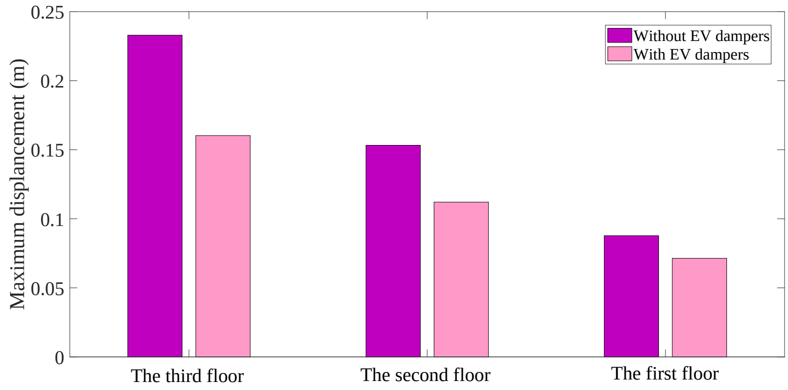

Figure 30. The maximum displacement of each floor in the Taft earthquake.

It can be seen that the structure with VE dampers has good seismic performance at the ambient temperature $T = 7.3$ °C. Indeed, compared with the case without VE dampers, VE dampers reduce the maximum displacement of each floor by more than 45.4%, 36.67%, and 22.97%, respectively, in the El Centro earthquake. Moreover, the maximum displacement decreases by more than 20.5%, 29.84%, and 11.53% under Taft wave excitation, respectively.

It is obvious that VE dampers are effective for seismic reduction, and the proposed AEF-Zener model can be applied to the analysis of the seismic performance and the design of structures with VE dampers in consideration of ambient temperature.

8. Conclusions

A new AEF-Zener model of VE dampers that takes into account temperature and the fractional-order equivalence principle was proposed. Firstly, the relationship between fractional order and energy dissipation of VE materials was analyzed in the time and frequency domains. Secondly, based on experimental data, the relationship between ambient temperature and energy dissipation of VE materials was analyzed. Finally, with the equivalence principle of temperature and fractional order, a new model able to describe the influence of temperature was established, and the model parameters were determined using a CFOPSO algorithm. Comparing the numerical results of the new AEF-Zener model with those of other models and with experimental data, it was shown that the proposed AEF-Zener model has good accuracy and availability, particularly in characterizing the loss factor for energy consumption. The proposed AEF-Zener model can be applied to design VE dampers in consideration of ambient temperature.

Author Contributions: Methodology, L.C.; software, M.Z.; validation and data curation, R.W.; writing—original draft preparation, K.X.; writing—review and editing, A.M.L.; supervision and project administration, M.W. All authors have read and agreed to the published version of the manuscript.

Funding: This work was supported by the National Natural Science Foundation of China (No. 62073114; 11971032).

Data Availability Statement: Data available on request due to restrictions eg privacy or ethical.

Conflicts of Interest: The authors declare no conflict of interest.

References

1. Huang, J.; Rao, Y.; Qiu, H.; Lei, Y. Generalized algorithms for the identification of seismic ground excitations to building structures based on generalized Kalman filtering under unknown input. *Adv. Struct. Eng.* **2020**, *23*, 2163–2173. [CrossRef]
2. He, Q.; Yin, A.; Fan, Z.; He, L. Seismic responses analysis of multi-story suspended floors system. *J. Vibroeng.* **2021**, *23*, 167–182. [CrossRef]
3. Gómez, F.; Yu, W. Discrete-time tri-directional active control of building structures. *Eng. Struct.* **2021**, *243*, 112689. [CrossRef]
4. Xu, K.; Chen, L.; Wang, M.; Lopes, A.M.; Tenreiro Machado, J.; Zhai, H. Improved decentralized fractional PD control of structure vibrations. *Mathematics* **2020**, *8*, 326. [CrossRef]

5. Hu, W.; Gao, Y.; Yang, B. Semi-active vibration control of two flexible plates using an innovative joint mechanism. *Mech. Syst. Signal Process.* **2019**, *130*, 565–584. [CrossRef]
6. Nasab, M.S.E.; Kim, J. Fuzzy analysis of a viscoelastic damper in seismic retrofit of structures. *Eng. Struct.* **2022**, *250*, 113473. [CrossRef]
7. Ocak, A.; Nigdeli, S.M.; Bekdaş, G. Passive control via mass dampers: A review of state-of-the-art developments. *Optimization of Tuned Mass Dampers*; Springer: Cham, Switzerland, 2022; pp. 15–40.
8. Stanikzai, M.H.; Elias, S.; Chae, Y. Recent advances in hybrid vibration-control systems. *Pract. Period. Struct. Des. Constr.* **2022**, *27*, 03122003. [CrossRef]
9. Feudo, S.L.; Touzé, C.; Boisson, J.; Cumunel, G. Nonlinear magnetic vibration absorber for passive control of a multi–storey structure. *J. Sound Vib.* **2019**, *438*, 33–53. [CrossRef]
10. Xu, Z.D.; Dong, Y.R.; Chen, S.; Guo, Y.Q.; Li, Q.Q.; Xu, Y.S. Development of hybrid test system for three-dimensional viscoelastic damping frame structures based on Matlab-OpenSees combined programming. *Soil Dyn. Earthq. Eng.* **2021**, *144*, 106681. [CrossRef]
11. Mokhtari, M.; Permoon, M.; Haddadpour, H. Dynamic analysis of isotropic sandwich cylindrical shell with fractional viscoelastic core using Rayleigh–Ritz method. *Compos. Struct.* **2018**, *186*, 165–174. [CrossRef]
12. Xu, Y.; Xu, Z.D.; Guo, Y.Q.; Dong, Y.; Ge, T.; Xu, C. Tests and modeling of viscoelastic damper considering microstructures and displacement amplitude influence. *J. Eng. Mech.* **2019**, *145*, 04019108. [CrossRef]
13. Dadkhah Khiabani, E.; Ghaffarzadeh, H.; Shiri, B.; Katebi, J. Spline collocation methods for seismic analysis of multiple degree of freedom systems with visco-elastic dampers using fractional models. *J. Vib. Control* **2020**, *26*, 1445–1462. [CrossRef]
14. Asano, M.; Masahiko, H.; Yamamoto, M. The experimental study on viscoelastic material dampers and the formulation of analytical model. In Proceedings of the 12th World Conference on Earthquake Engineering, Nagoya, Japan, 30 January–4 February 2000.
15. Barkanov, E.; Skukis, E.; Petitjean, B. Characterisation of viscoelastic layers in sandwich panels via an inverse technique. *J. Sound Vib.* **2009**, *327*, 402–412. [CrossRef]
16. Hamdaoui, M.; Ledi, K.; Robin, G.; Daya, E.M. Identification of frequency-dependent viscoelastic damped structures using an adjoint method. *J. Sound Vib.* **2019**, *453*, 237–252. [CrossRef]
17. Dadkhah, E.; Shiri, B.; Ghaffarzadeh, H.; Baleanu, D. Visco-elastic dampers in structural buildings and numerical solution with spline collocation methods. *J. Appl. Math. Comput.* **2020**, *63*, 29–57. [CrossRef]
18. Xu, Z.D.; Liao, Y.X.; Ge, T.; Xu, C. Experimental and theoretical study of viscoelastic dampers with different matrix rubbers. *J. Eng. Mech.* **2016**, *142*, 04016051. [CrossRef]
19. Shu, Z.; You, R.; Zhou, Y. Viscoelastic Materials for Structural Dampers: A Review. *Constr. Build. Mater.* **2022**, *342*, 127955. [CrossRef]
20. Zhang, X.; Wu, R.C. Modified projective synchronization of fractional-order chaotic systems with different dimensions. *Acta Math. Appl. Sin. Engl. Ser.* **2020**, *36*, 527–538. [CrossRef]
21. Xu, Z.D.; Ge, T.; Liu, J. Experimental and theoretical study of high-energy dissipation-viscoelastic dampers based on acrylate-rubber matrix. *J. Eng. Mech.* **2020**, *146*, 04020057. [CrossRef]
22. Arikoglu, A. A new fractional derivative model for linearly viscoelastic materials and parameter identification via genetic algorithms. *Rheol. Acta* **2014**, *53*, 219–233. [CrossRef]
23. Xu, Y.; Xu, Z.D.; Guo, Y.Q.; Sarwar, W.; She, W.; Geng, Z.F. Study on viscoelastic materials at micro scale pondering supramolecular interaction impacts with DMA tests and fractional derivative modeling. *J. Appl. Polym. Sci.* **2023**, *140*, e53660. [CrossRef]
24. Sun, H.; Zhang, Y.; Baleanu, D.; Chen, W.; Chen, Y. A new collection of real world applications of fractional calculus in science and engineering. *Commun. Nonlinear Sci. Numer. Simul.* **2018**, *64*, 213–231. [CrossRef]
25. Bonfanti, A.; Kaplan, J.L.; Charras, G.; Kabla, A. Fractional viscoelastic models for power-law materials. *Soft Matter* **2020**, *16*, 6002–6020. [CrossRef] [PubMed]
26. Markou, A.A.; Manolis, G.D. A fractional derivative Zener model for the numerical simulation of base isolated structures. *Bull. Earthq. Eng.* **2016**, *14*, 283–295. [CrossRef]
27. Rodas, C.O.; Zaïri, F.; Naït-Abdelaziz, M. A finite strain thermo-viscoelastic constitutive model to describe the self-heating in elastomeric materials during low-cycle fatigue. *J. Mech. Phys. Solids* **2014**, *64*, 396–410. [CrossRef]
28. Lewandowski, R. Influence of temperature on the dynamic characteristics of structures with viscoelastic dampers. *J. Struct. Eng.* **2019**, *145*, 04018245. [CrossRef]
29. Xu, Y.; Xu, Z.D.; Guo, Y.Q.; Ge, T.; Xu, C.; Huang, X. Theoretical and experimental study of viscoelastic damper based on fractional derivative approach and micromolecular structures. *J. Vib. Acoust.* **2019**, *141*, 031010. [CrossRef]
30. Ge, T.; Xu, Z.D.; Guo, Y.Q.; Huang, X.H.; He, Z.F. Experimental investigation and multiscale modeling of ve damper considering chain network and ambient temperature influence. *J. Eng. Mech.* **2022**, *148*, 04021124. [CrossRef]
31. Cao, J.; Chen, Y.; Wang, Y.; Zhang, H. Numerical analysis of nonlinear variable fractional viscoelastic arch based on shifted Legendre polynomials. *Math. Methods Appl. Sci.* **2021**, *44*, 8798–8813. [CrossRef]
32. Sun, L.; Chen, Y. Numerical analysis of variable fractional viscoelastic column based on two-dimensional Legendre wavelets algorithm. *Chaos Solitons Fractals* **2021**, *152*, 111372. [CrossRef]

33. Moghaddam, B.; Mendes Lopes, A.; Tenreiro Machado, J.; Mostaghim, Z. Computational scheme for solving nonlinear fractional stochastic differential equations with delay. *Stoch. Anal. Appl.* **2019**, *37*, 893–908. [CrossRef]
34. Ortigueira, M.D.; Machado, J.T. The 21st century systems: An updated vision of continuous-time fractional models. *IEEE Circuits Syst. Mag.* **2022**, *22*, 36–56. [CrossRef]
35. Ortigueira, M.D.; Valério, D. *Fractional Signals and Systems*; Walter de Gruyter GmbH & Co KG: Berlin, Germany, 2020; Volume 7.
36. Ortigueira, M.D. *Fractional Calculus for Scientists and Engineers*; Springer Science & Business Media: Berlin/Heidelberg, Germany, 2011; Volume 84
37. Majidabad, S.S.; Shandiz, H.T.; Hajizadeh, A. Decentralized sliding mode control of fractional-order large-scale nonlinear systems. *Nonlinear Dyn.* **2014**, *77*, 119–134. [CrossRef]
38. Xiao, M.; Tao, B.; Zheng, W.X.; Jiang, G. Fractional-order PID controller synthesis for bifurcation of fractional-order small-world networks. *IEEE Trans. Syst. Man Cybern. Syst.* **2019**, *51*, 4334–4346. [CrossRef]
39. Yuan, J.; Gao, S.; Xiu, G.; Wang, L. Mechanical energy and equivalent viscous damping for fractional Zener oscillator. *J. Vib. Acoust.* **2020**, *142*, 041004. [CrossRef]
40. Shahri, E.S.A.; Alfi, A.; Machado, J.T. Fractional fixed-structure H_∞ controller design using augmented Lagrangian particle swarm optimization with fractional order velocity. *Appl. Soft Comput.* **2019**, *77*, 688–695. [CrossRef]
41. Wang, C.; Zhou, X.; Jin, Y.; Shi, X. Variable fractional order sliding mode control for seismic vibration suppression of building structure. *J. Vib. Control.* **2022**, *28*, 3794–3807. [CrossRef]
42. Li, H.; Gomez, D.; Dyke, S.J.; Xu, Z. Fractional differential equation bearing models for base-isolated buildings: Framework development. *J. Struct. Eng.* **2020**, *146*, 04019197. [CrossRef]
43. Xu, K.; Cheng, T.; Lopes, A.M.; Chen, L.; Zhu, X.; Wang, M. Fuzzy Fractional-Order PD Vibration Control of Uncertain Building Structures. *Fractal Fract.* **2022**, *6*, 473. [CrossRef]
44. Zheng, Y.; Huang, Z.; Tao, J.; Sun, H.; Sun, Q.; Sun, M.; Dehmer, M.; Chen, Z. A novel chaotic fractional-order beetle swarm optimization algorithm and its application for load-frequency active disturbance rejection control. *IEEE Trans. Circuits Syst. II Express Briefs* **2021**, *69*, 1267–1271. [CrossRef]
45. Xu, Y.; Xu, Z.D.; Guo, Y.Q.; Jia, H.; Huang, X.; Wen, Y. Mathematical modeling and test verification of viscoelastic materials considering microstructures and ambient temperature influence. *Mech. Adv. Mater. Struct.* **2021**, *29*, 7063–7074. [CrossRef]